Nuclear Instruments and Methods 203 (1982) 119–127
North-Holland Publishing Company

THE CENTRAL DRIFT CHAMBER FOR THE HIGH RESOLUTION SPECTROMETER AT PEP *

D. RUBIN, J. CHAPMAN, D. NITZ, A. SEIDL and R. THUN **
Department of Physics, University of Michigan, Ann Arbor, MI 48109, USA

Received 20 October 1981 and in revised form 1 April 1982

The central drift chamber of the High Resolution Spectrometer (HRS) at PEP is described. Results on efficiency, calibrations and resolution are given for magnetic fields up to 1.6 T.

1. Introduction

A large cylindrical drift chamber is the main tracking device for the High Resolution Spectrometer (HRS) at PEP. The general layout of the HRS is shown in fig. 1. The drift chamber axis coincides with the beam line as well as the symmetry axis of the magnet, and its midpoint is centered on the crossing point of the electron and positron bunches. The chamber contains 2448 drift cells arranged in fifteen concentric layers. Wires of seven of the layers are oriented axially (z) and the remaining eight (u, v) at small angles with respect to the cylinder axis. The drift chamber geometry permits charged particle tracking over 90% of 4π sr solid angle. Fig. 2 shows a side view of the chamber and table 1 summarizes the geometry. As indicated in fig. 1, the tracking system of the HRS is completed by the addition of two layers of axially oriented drift tubes at large radius ($r = 189$ cm). These provide increased resolution at high momentum. The design and performance of these drift tubes is described elsewhere [1].

Important aspects of the central drift chamber design are its light structure and the capability to operate in magnetic fields up to 1.6 T. To preserve the excellent momentum resolution provided by the high magnetic field a major effort was made to minimize multiple scattering. The use of beryllium and aluminum honeycomb in the drift chamber structure have limited the thickness of the chamber for traversing particles to 0.020 radiation lenghts. The capability to operate in high magnetic fields is achieved with a simple cell geometry by limiting the cell width (and hence maximum drift distance) while keeping a relatively large cell depth to allow containment of ionization electrons drifting at large angles to the electric drift field.

The completed HRS, including the central drift chamber, has been tested extensively with cosmic rays. Since October 1981, the spectrometer has been recording physics data at PEP. We describe here results from cosmic ray and PEP data which show that the drift chamber operates with high resolution, effciency and reliability.

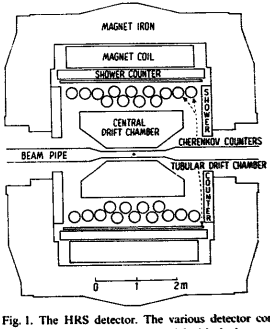

Fig. 1. The HRS detector. The various detector components follow a cylindrical geometry coaxial with the beam pipe.

2. Geometry

The general layout of drift cells is indicated in fig. 3 and table 1. Each layer consists of a ring of cells with a minimal number of wires, one sense and three field wires per cell. Earlier tests had shown that such a simple cell geometry yielded good efficiency and resolution in high magnetic fields [2]. The choice of cell size was

* Work supported by the U.S. Department of Energy.
** Supported in part by the Alfred P. Sloan Foundation.

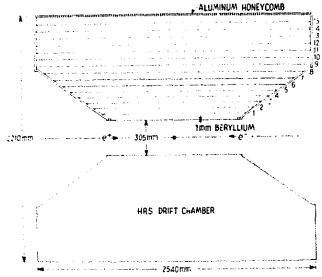

Fig. 2. Side view of the central drift chamber. The sense wires of the 15 layers are indicated in the upper half of the drawing.

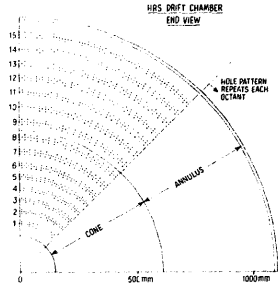

Fig. 3. End view of the central drift chamber showing an octant of the drift cell geometry.

constrained by three considerations. First, it was decided to limit the maximum width to about 2.5 cm to assure full efficiency with reasonable drift times at high magnetic fields. Second, some attempt was made to preserve good segmentation at the smaller radii by reducing the cell width at those radii. And third, an eight-fold symmetry was imposed to facilitate the design of electrical connections and various survey checks. The resulting variation of cell size with layer increases the number of calibration constants for the drift chamber. However, this increase has not presented any special difficulty.

All even-numbered of the fifteen drift chamber layers are oriented axially (z). Odd-numbered layers alternate with positive and negative angles of approximately ± 60 mrad with respect to the cylinder axis. The combination of axial and angled wires allows the full three-dimensional reconstruction of particle tracks. The angles of odd-numbered layers were determined by stringing wires within a layer from cell N at one end to cell $N + \Delta N$ at the opposite end of the chamber where $\Delta N = \pm 5$ or 6 as indicated in table 1.

3. Mechanical design and construction

The major structural components are shown in fig. 4. Each end consists of a cone and an annulus which are

Table 1
Geometry of drift chamber

Layer	Radius (cm)	Number of cells	Cell size (cm)	Orientation	Cell shift	Angle (mrad)
1	20.96	80	1.65	u	+5	+61.7
2	26.04	96	1.70	z	0	0
3	31.12	112	1.74	v	−6	−64.5
4	36.20	128	1.78	z	0	0
5	41.28	144	1.80	u	+6	+56.6
6	46.36	144	2.02	z	0	0
7	52.07	144	2.27	v	−6	−61.4
8	58.42	144	2.55	z	0	0
9	64.77	160	2.54	u	+6	+60.2
10	71.12	176	2.54	z	0	0
11	77.47	192	2.53	v	−6	−60.0
12	83.82	208	2.53	z	0	0
13	90.17	224	2.53	u	+6	+59.9
14	96.52	240	2.53	z	0	0
15	102.87	256	2.53	v	−6	−59.8

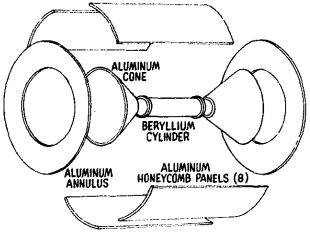

Fig. 4. Major structural components of the central drift chamber.

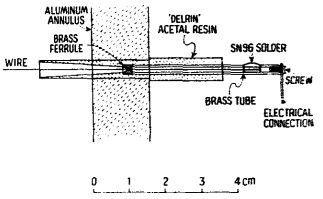

Fig. 5. Schematic of pin design for sense and field wires.

bolted together. The annulus is 1.59 cm thick cast aluminium plate, and the cone is cast aluminium [3] machined to a wall thickness of 0.95 cm. Pins holding the 9792 drift chamber wires were located by 0.516 cm diameter holes drilled into the annuli and cones [4]. Flats were milled on the cones prior to the drilling of holes to allow proper seating of the pins. The hole pattern, which has 8-fold symmetry, is shown in fig. 3. Several hundred measurements of hole locations have shown their relative position to be typically within 25 to 50 μm of specification.

The two drift chamber ends are separated by a 119.4 cm long beryllium cylinder [5] with a diameter of 30.5 cm and a wall thickness of 1 mm. Beryllium, despite its high cost, was chosen because it minimizes multiple scattering and photon conversion. In addition, beryllium is a very stiff metal. Indeed, the beryllium cylinder and aluminum cones hold their fraction of the total wire tension of 30000 N with negligible compressive strain. Thus no elaborate prestressing or post-tensioning techniques were needed to maintain wire tension.

The cylinder is closed at the outer radius by a set of eight identical aluminum honeycomb panels. The panels are individually removable to allow access to the interior of the chamber. During the wire-stringing phase all panels were removed and replaced by eight aluminum bars of small (5×5 cm^2) cross section. The panels consist of 0.95 cm thick aluminum honeycomb sandwiched between 0.13 mm thick aluminum skins. Compressive forces from the wire tension are transmitted to the panels via set screws embedded in the aluminum annuli at their outer radius.

The pins holding the sense and field wires of the drift chamber are shown in fig. 5. Each pin consists of an insulating feed-through, a small brass ferrule for locating the wire, and a brass tube to which the wire is soldered. The feed-throughs were specified to be machined from Delrin [6] although a similar plastic Celcon [7] was substituted in the manufacture of a large number of the pins. Electrical problems associated with the use of these plastics will be described later. The brass ferrule has a 150 μm diameter hole which tapers outward to facilitate the threading of te wires. The brass tube has a slot for feeding in solder and is threaded at one end to allow easily removable electrical connections. All pins were optically scanned for concentricity of the ferrule hole. Sense wire pins were required to show concentricity to better that 50 μm.

Sense wires consist of 37 μm diameter gold-plated tungsten. Tungsten was chosen for its great mechanical strength. The field wires are 125 μm diameter gold-plated beryllium copper. Wires were strung according to the following procedure. First each wire was threaded through the pins and clamped to a post outside one end of the drift chamber cylinder. The wire at the other end was then pulled over a low-friction wheel and attached to a weight to provide the proper tension (140 g for sense and 360 g for field wires). When tensioned, wires were pulled radially inward toward the drift chamber axis so that the position uncertainty is smaller than the ferrule hole diameter. Both wire ends were then resistance-soldered to their respective brass tubes described above. The resistance-soldering technique provided a very fast, uniform method for bonding the wires to the tubes. By tensioning the entire length of wire before soldering and by using SN96 silver–tin solder, potential problems with solder creep appear to have been eliminated. (None of the 9792 wires have pulled out of their solder in the two years since construction was completed.)

The beryllium–copper field wires are quite "stretchy" in that they exhibit 20% elongation beyond the elastic limit. This elongation is critical to our technique for replacing individual wires [8]. To replace a defective field wire, one of its ends is gently stretched by pulling the associated pin from its hole. A new wire is attached and drawn into the drift chamber by pulling on the other end of the defective wire. Sense wire replacement is somewhat more complicated since tungsten cannot be

stretched sufficiently without breaking. In this case, a neighboring field wire is used to pull through a new sense wire and a replacement field wire. The sense wire is then hooked into its own hole at each end. Needless to say, this is a more delicate operation.

The choice of wire tensions given above is a compromise between remaining well below the elastic limit and minimizing gravitational sag. The maximum gravitational deflection for the longest sense wires is 115 μm. For the field wires it is 250 μm.

4. Signal readout and high voltage distribution

The collection of raw signals as well as the distribution of negative high voltage is achieved with circuit boards mounted between drift-cell layers at one end of the chamber. Each board, shown in fig. 6, serves 16 cells. On the side facing the chamber, the signal pads are connected to a multipin connector via traces which are separated by ground traces to minimize cross talk. The signals are transmitted from the connector to preamplifiers mounted on the magnet iron via 6.7 m long coaxial ribbon cable.

The high voltage between sense and field wires is established by placing positive high voltage on the sense wires and an equal magnitude of negative high voltage on the field wires. The sense wire signal is decoupled from the high voltage with a 100 pF capacitor. The initial design had foreseen keeping the sense wires at ground potential but a serious problem with the insulating feed-throughs of the pins forced a splitting of the voltage. During early testing of the completed chambers, when all the high voltage was applied to the field wires only, a rather high rate of large noise pulses was observed on the sense wires. After an extensive investigation, it was deduced that the pulses were associated with discharges between field wires and the plastic interior of the pins in the high electric-field region where the pins pass through the grounded aluminum

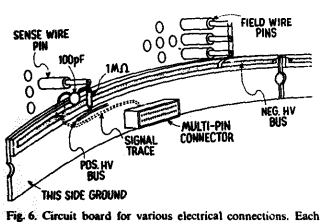

Fig. 6. Circuit board for various electrical connections. Each board serves 16 cells in a given layer.

structure of the drift chamber. After the charge leaked off the plastic, the discharge would repeat and be seen on all sense wires. The problem was worse for some layers than for others. Further investigation showed that Celcon was substituted for Delrin during the manufacture of many of the insulating feed-throughs. Celcon is very similar to Delrin except that it has a much lower resistivity, by a factor of 100 or so. The charge in the Celcon pins would thus bleed off much faster inducing a high rate of discharges. The resulting noise problem was reduced to negligible proportions by splitting the high voltage as described above. In effect, this action reduced the discharge-inducing electric field by a factor of two. (In retrospect, the discharge problem could also have been avoided if the pins had been designed so as to shield the wires with the brass tube through the entire thickness of the aluminum structure.) In addition to solving the discharge problem, the reduced split voltages also had the unforeseen but fortuitous effect of largely eliminating noise from external corona discharges observed earlier in operation at high humidity.

5. Electronics

Raw sense wire signals are sent to LeCroy DC201A amplifier-discriminator units via 6.6 m long, 93 Ω coaxial ribbon cable [9]. These input signals are terminated with 100 Ω and balanced with 100 Ω between the shield and the positive input of the differential preamplifier as shown in fig. 7. This symmetric coupling of the shield to both the positive and negative inputs of the preamps suppresses shield-noise through the common mode rejection of the preamps. Output pulses from the DC201A are transmitted to time digitizers (TDC's) through 23 or 31 m long twisted-pair ribbon cable [10]. The DC201A's are mounted in twelve cages outside the magnet iron for easy access. A test circuit is a permanent feature of each cage through which a time and amplitude controlled signal can be injected into all preamps simultaneously. With this test feature the time skewing and threshold sensitivity of each channel can be established regularly as a diagonistic feature.

Drift times are measured with a TDC system developed and fabricated at the University of Michigan [11]. A major feature of the system is that drift times are digitized by use of a common clock which assures a

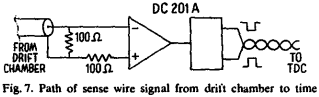

Fig. 7. Path of sense wire signal from drift chamber to time digitizer (TDC).

highly stable operation of the system. Each TDC module contains eight channels and is packaged using standard single-width CAMAC hardware. Each channel has an eight-bit measurement range and operates at clock frequencies up to 100 MHz. Both edges of every clock pulse are counted to give a minimum period of 5 ns, equivalent to an rms time resolution of less than 1.5 ns. The actual clock frequency of 85 MHz was chosen so that the time range of the TDC exceeds the maximum drift times observed when operating at 1.6 T magnetic field. Time measurements begin when the beam crossing signal initiates the generation of a fixed number of clock pulses. During these clock pulses a gate is generated and sent to all TDC's. The arrival of a preamp output pulse at an individual TDC channel during the gate period sets the active bit in that particular channel. All clock edges occurring after the active bit is set are counted. This sequence of time counting reduces power consumption since the majority of channels, which are empty in a typical event, will not be counting clock pulses.

Each crate of TDC modules contains a controller unit which manages the readout of the TDC's in its crate. The controller units are connected by a readout bus to a single interface module which controls the readout of the TDC system and various test and calibration features. The TDC information is encoded with the station and channel address. Empty channels are not read. The TDC design has two features specifically designed for trigger information output. The first feature provides the logical "OR" of all channel active bits within an 8-channel TDC module. The second provides the active-bit information within a module through an eight-bit shift register accessible from the front panel of the TDC. These outputs constitute the data for the fast (2 μs) and intermediate (30 μs) triggers of the spectrometer, respectively.

6. Drift chamber gas

The drift chamber gas is a premixed combination of 89% argon, 10% carbon dioxide and 1% methane [12]. This mixture has a number of important advantages. First, it is a safe gas in terms of fire hazard and requires no elaborate venting precautions. Second, it does not form whisker-like deposits on wires when a drift chamber is operated with high electric fields and at high radiation levels [13]. Although drift velocities are not saturated with this gas in the low electric field regions of the drift cells, this presents no additional problem since operation in high magnetic fields already imposes a fairly complicated time-to-distance relationship. The one percent methane component was not needed by the central drift chamber but was added to improve the performance of the tubular drift chambers.

The gas is distributed in the chamber by a manifold consisting of a thin torus attached to the inner face of one of the aluminum annuli at large radius. Thirty-two evenly-spaced 1 mm diameter holes feed gas into the chamber volume. There are four low-impedance exhaust ports on the opposite annulus. Overall gas tightness of the drift chamber is provided by O-rings at cone–annulus and cone–beryllium cylinder interfaces and by epoxy-covered glass tape elsewhere. The exhaust gas can be checked with either a simple small proportional wire chamber attached to one of the four exhaust ports or by a more elaborate gas velocity monitor [14]. No attempt is made to purify and recirculate the gas.

7. Measurements of drift chamber efficiency

The drift chamber has been tested with cosmic rays and PEP data in magnetic fields ranging from zero to 1.6 T. The chamber and associated electronics have operated with great reliability. Typically only a small number (< 5) of drift cell channels are electronically inoperative at any given time.

Drift layer efficiencies were measured as a function of the total high voltage between sense and field wires. These measurements were made simply by varying the high voltage on a given layer and counting the fraction of events where the layer did not contribute an appropriate signal to a particle track. Results for zero and 1.6 T magnetic fields are shown in fig. 8 for layers with small and large cells. It is noted that the efficiency curve at 1.6 T is shifted approximately 50 V higher relative to the one at zero field. The efficiency is better than 99%

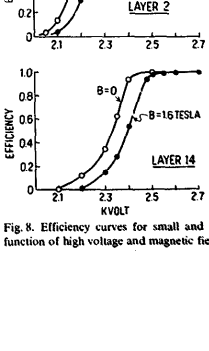

Fig. 8. Efficiency curves for small and large drift cells as a function of high voltage and magnetic field.

over the full range 0–1.6 T for all layers. The plateaus extend several hundred volts before appreciable currents are drawn by the drift chamber. It is therefore possible to operate the drift chamber with one set of high voltages over the full range of magnetic fields, 0–1.6 T. The voltage ranges from 2500 KV for layers with small cells to 2650 KV for those with the largest cells.

8. Time–space calibrations

The calibration of the drift chamber is somewhat complex since drift times have a strong dependence on magnetic field and the angle of incidence of tracks. We report here experimental results and compare them to those obtained from a simple model which is in good agreement with the data.

8.1. A model for generating drift chamber calibrations

A simple model [15], which reproduces drift chamber response in a coaxial magnetic field quite well, parameterizes the drift velocity of electrons as follows:

$$V_{\parallel} = \frac{V_0}{1 + (V_0 B/KE)^2}, \tag{1}$$

$$V_{\perp} = \frac{V_0 B}{KE} V_{\parallel}, \tag{2}$$

where $V_{\parallel}$ and $V_{\perp}$ are drift velocity components parallel and perpendicular to the electric drift field inside the cell. The parameter V_0 is the magnitude of the drift velocity when the magnetic field, B, is zero. The electric field is given by E, and K is an empirical parameter

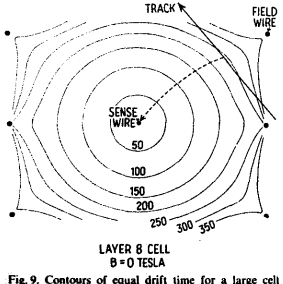

Fig. 9. Contours of equal drift time for a large cell at zero magnetic field. The dashed line indicates the electron drift path. Drift times are given in ns.

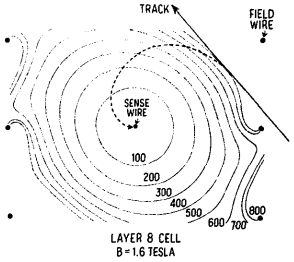

Fig. 10. Contours of equal drift for the same cell with a 1.6 T magnetic field.

which, in general, depends on E. We have calculated drift times with this model without resorting to adjustable parameters by using independent measurements of V_0 and K as a function of E [16]. The electric field E is calculated for any point in a drift cell by using as input the geometry and high voltages of the drift chamber. The only approximations used in the calculation of E are the assumption of a uniform surface charge density on a given wire and the inclusion of only a finite number of neighboring cells in the calculation.

We are able to determine with this model the earliest arrival time of ionization electrons for tracks passing through a drift cell at arbitrary distances of closest approach to the sense wire and with arbitrary angles of incidence. Results obtained by model calculations are shown in figs. 9 and 10 which display contours of equal drift time in a large drift cell for $B = 0$ and $B = 1.6$ T. It is interesting to note that at large distances from the sense wire, drift times increase by roughly a factor of 2.5 when B is increased from 0 to 1.6 T. In addition the magnetic field introduces an asymmetry in drift times between the two sets of diagonal corners. This in turn introduces an asymmetry in the drift chamber calibrations between tracks of positive and negative angles of incidence.

8.2. Experimental results and comparison with model

We have recorded several million cosmic ray tracks in magnetic fields ranging from zero to 1.6 T. Even at PEP cosmic rays provide the most copious source of easily analyzed tracks. For this analysis of drift chamber response versus magnetic field we require that cosmic ray tracks pass within 4 cm of the chamber axis and that the tracks be reasonably straight so that the angle of

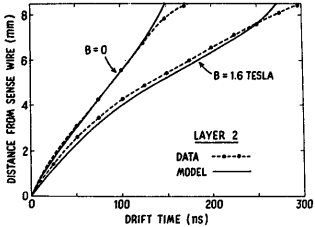

Fig. 11. Time-to-space calibration for perpendicularly incident tracks for a small cell at zero magnetic field and at 1.6 T.

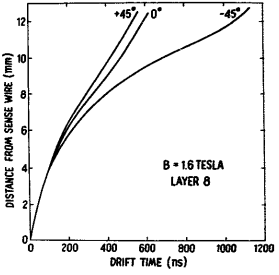

Fig. 13. Time-to-space calibration for three angles of incidence.

incidence in all layers is nearly perpendicular. The latter requirement was equivalent to selecting tracks with greater than 5 GeV/c momentum for measurements with non-zero magnetic fields.

A time-to-space calibration is then obtained, in the approximation of uniform particle flux across a drift cell, by integrating the drift time distributions dN/dt as follows:

$$x(t) = x_{max}\left[\int_0^t \frac{dN(t')}{dt'}\,dt'\right] \Big/ \left[\int_0^{t'_{max}} \frac{dN(t')}{dt'}\,dt'\right], \quad (3)$$

where x_{max} is the maximum drift distance corresponding to the maximum drift time t_{max}. For perpendicularly incident tracks, as selected here, x_{max} is equal to half the cell width. Across a typical cell, the cosmic ray flux is uniform to within a few percent so that the above relationship is expected to give an accurate calibration. The time-to-space calibrations obtained in this manner are shown in figs. 11 and 12 for small and large cells and for $B = 0$ and $B = 1.6$ T.

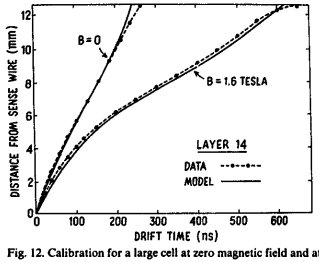

Fig. 12. Calibration for a large cell at zero magnetic field and at 1.6 T.

For comparison, the calibration calculated purely from the model described in the previous section is also shown. The agreement is quite impressive with average deviations between measurement and model at the 200 μm level. Larger deviations are observed near the edge of the cell. These deviations are caused by the rapid variation of drift times at the cell boundary. Since real tracks exhibit a finite spread in the angle of incidence, one obtains a smearing of drift times for a given distance from the sense wire. This smearing tends to flatten the empirical calibration curves near the cell edge. The calibration curves are fitted well by fourth-order polynomials of the drift time.

The time-space relationship changes as the angle of incidence of a track varies with respect to the cell orientation. Fig. 13 shows results obtained from the model at $B = 1.6$ T and angles of $\pm 45°$. The calibration for perpendicular ($\theta = 0°$) tracks is shown for comparison.

9. Spatial resolution

The calibration data also yield measurements of the spatial resolution of the drift chamber. Helical trajectories are fit to the data using the calibration found by the procedure described above. To minimize the effect of multiple scattering, tracks with momenta above 5 GeV/c are selected for the analysis. Fig. 14 shows a typical distribution of the difference between measured and fitted coordinates for one of the drift cell layers at $B = 1.6$ T. The average width at half maximum of all layers is ± 250 μm. An analysis of data with zero

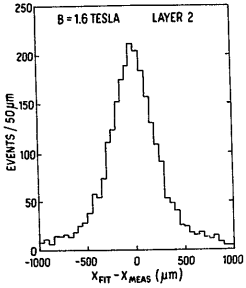

Fig. 14. Typical distribution of deviations between fitted and measured track coordinates from a preliminary analysis of cosmic ray data.

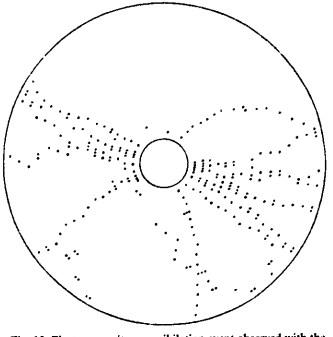

Fig. 15. Electron–positron annihilation event observed with the central drift chamber at PEP.

magnetic field yields similar results indicating that the high magnetic field does not degrade resolution.

The 250 μm measurement uncertainty includes contributions from the intrinsic resolution (< 200 μm), sense wire placement errors (~ 50 μm), gravitational sag (< 115 μm), electronic resolution (< 50 μm) and uncertainties from both magnetic field non-uniformity and calibration procedures which are difficult to estimate. It is expected that with further experience the resolution can be improved to the 200 μm level.

10. Summary

The central drift chamber of the HRS has operated at PEP in magnetic fields up to 1.6 T. It has performed with a high degree of reliability. At 1.6 T, drift cell efficiency exceeds 99% and initial calibration efforts yield spatial resolutions around ±250 μm. Table 2 summarizes the characteristics of the drift chamber. The response of the chamber to a typical electron–positron annihilation event is shown in fig. 15.

A large effort such as the construction of this drift chamber system involves the work of many. We express our deep appreciation for the enthusiastic and competent support received from the University of Michigan machine and electronics shops. We are also grateful for the outstanding quality of the machining work performed by the Alliance Tool and Die Corporation. We

Table 2
Summary

Geometry	cylindrical with 7 axial and 8 small-angle layers
Number of cells	2448
Number of wires	1 sense and 3 field wires per cell
Sense wire	37 μm gold-plated tungsten
Field wire	127 μm gold-plated beryllium–copper
Gas	89% argon, 10% CO_2, 1% CH_4
Amplifier-discriminator	LRS D2201A
Time-to-digital converter	D. Nitz digital design
High voltage	2500–2650 V depending on cell (inner and outermost layers somewhat higher)
Efficiency	>99% for $B = 0$ to 1.6 T
Drift times	~650 ns at $B = 1.6$ T for maximum drift distance of 1.27 cm
Resolution	±250 μm at $B = 0$ and 1.6 T

thank Professor D. Meyer for his help in the fabrication of the honeycomb panels, and finally, our thanks go to those who assembled 20000 pins and threaded and soldered 100Ω wires!

References

[1] G. Baranko et al., Nucl. Instr. and Meth. 169 (1980) 413.
[2] R.P. Thun and P. Kraushaar, Measurement of drift chamber performance in high magnetic fields, University of Michigan Memo UM HE 77-47.
[3] Castings were made by Frontier Bronze Corporation of Niagara Falls, New York.
[4] The machining of the cones and annuli, including the drilling of holes, was performed by Alliance Tool and Die Corporation of Rochester, New York.
[5] The beryllium cylinder was manufactured by Electrofusion Corporation of Menlo Park, California.
[6] Delrin is an acetal resin manufactured by Dupont. Volume resistivities vary from 5×10^{14} to 2.66×10^{16} Ω cm.
[7] Celcon is an acetal copolymer produced by Celanese. Volume resistivity is 10^{14} Ω cm.
[8] Our technique of wire replacement is based on that developed by the Mark II collaboration at SLAC.
[9] The cable is 17-conductor coaxial ribbon cable manufactured by AMP. The cable has given some problems involving the creep of conducting wires relative to the insulator.
[10] The cable is Spectra Strip "Twist-n-Flat" containing eight pairs of conductors.
[11] D. Nitz, A digital drift chamber digitizer system, Proc. IEEE 1978 Nuclear Science Symposium.
[12] D. Koltick, Gas studies in the outer drift chambers, Internal HRS Memo 197.
[13] A. Odian, private communication describing tests done by the MKIII collaboration at SLAC.
[14] G. Baranko, The drift velocity monitor, Internal HRS Memo 198.
[15] See ref. 1.
[16] We have used values for V_0 and K as a function of E as given by refs. 1 and 14.